

Epitaxial ZnO Layer Growth on Si(111) Substrates with an Intermediate AlN Nucleation Layer by Methane-Based Chemical Vapor Deposition

Raphael Müller,* Okan Gelme, Jan-Patrick Scholz, Florian Huber, Manuel Mundsinger, Yueliang Li, Manfred Madel, Alexander Minkow, Ute Kaiser, Ulrich Herr, and Klaus Thonke



Cite This: <https://dx.doi.org/10.1021/acs.cgd.0c00907>



Read Online

ACCESS |



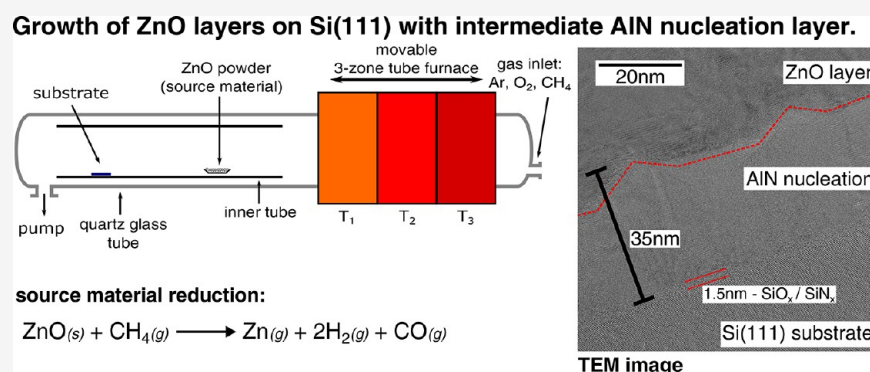
Metrics & More



Article Recommendations



Supporting Information



ABSTRACT: The growth of high-quality single-crystalline zinc oxide (ZnO) layers on silicon (Si(111)) substrates with an intermediate aluminum nitride (AlN) nucleation layer was investigated. The ZnO layers were grown using a methane (CH_4)-based chemical vapor deposition (CVD) growth process, while the AlN nucleation layers were grown by metal–organic vapor-phase epitaxy (MOVPE). We investigate the influence of nucleation layer thickness and growth temperature on the final ZnO layer quality and also vary the ZnO growth parameters to obtain smooth surfaces and the best crystal quality. The ZnO layers were extensively characterized by various methods such as atomic force microscopy (AFM), high-resolution X-ray diffraction (HRXRD), electron backscatter diffraction (EBSD), and scanning/transmission electron microscopy (SEM/TEM). We find that AlN nucleation layers grown at 1150 °C for 15 min yielded the best final ZnO layer quality with fully c oriented ZnO layers free of rotational domains. In HRXRD ω scans full width of half maximum (fwhm) values of about 710 and 1240 arcsec for the (0002) and (10 $\bar{1}$ 2) reflections, respectively, were achieved. Dislocation densities of $\rho_{\text{edge}} = 1.6 \times 10^{10}$ and $\rho_{\text{screw}} = 9.1 \times 10^8 \text{ cm}^{-2}$ and a lateral coherence length (LCL) of $L_{\parallel} = 300 \text{ nm}$ are deduced, values which are among the best reported in the literature for ZnO layers grown on Si(111). Additionally, we carried out high-resolution photoluminescence (PL) measurements at liquid-helium and room temperatures, which also prove low defect densities. The low-temperature PL spectra were also used to study the stress within the ZnO layer and compared to HRXRD stress measurements. Both measurements confirm a stress reduction in the ZnO layer with increasing thickness.

INTRODUCTION

ZnO plays a special role in the family of wide-band-gap semiconductors. For decades it was considered as a promising material for optoelectronic devices in the near-UV spectral range. However, reproducible p-type doping has not been achieved by now, and theoretical calculations question if this is even possible.^{1–4} Still, ZnO is suited for a wide range of other applications: for example, as extremely sensitive gas sensors,⁵ surface acoustic wave (SAW) devices,⁶ unipolar thin-film transistors (TFT),⁷ and transparent conductive oxide (TCO) layers.⁸ Combining this large range of applications with Si-based integrated chip technology offers great opportunities. For this purpose the epitaxial growth of ZnO on Si has to be

well understood and controlled. In addition to the large lattice mismatch ($\sim 15.4\%$)⁹ and the huge difference in thermal expansion coefficients, the formation of an amorphous SiO_x interlayer at the initial stage of ZnO growth is a big challenge in this special case of heteroepitaxial growth. To prevent

Received: July 1, 2020

Revised: August 11, 2020

Published: August 11, 2020

oxidation, the Si substrate has to be covered before ZnO growth. Research on many different interlayer materials can be found in the literature, ranging from pure metals such as zinc^{10–12} and aluminum,¹³ to sulfides and oxides such as wurtzite ZnS,¹⁴ MgO,¹⁵ Al₂O₃,¹⁶ Lu₂O₃,¹⁷ Y₂O₃,⁹ Gd₂O₃(Ga₂O₃),¹⁸ and yttria-stabilized ZrO₂ (YSZ),¹⁹ and to nitrides such as GaN^{20,21} and AlN.^{6,22} Because the thermal expansion coefficient of AlN for the in-plane lattice constant in the temperature range of the growth process is between the values of ZnO and Si as shown in Table 1, it not only prevents

Table 1. Values used for the Calculation of Layer Stress

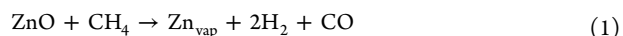
	<i>E</i> (GPa)	ν	α at 300 K (10 ⁻⁶ K ⁻¹)	α at 1000 K (10 ⁻⁶ K ⁻¹)	<i>d</i> (μ m)
ZnO	142 ⁵¹	0.3 ⁵¹	4.90 ⁵²	8.98 ⁵²	
Si	169 ⁵³	0.36 ⁵³	2.69 ⁵⁴	4.27 ⁵⁴	400

the Si surface from oxidation but also helps to overcome the mismatch in thermal expansion coefficient. Furthermore, we showed in previous reports that AlN nucleation can yield high-quality ZnO layers on sapphire substrates for methane-based CVD growth.^{23,24} Some of the aforementioned applications may benefit from a novel growth method for high-quality ZnO layers introduced by Huber et al.²³ This CVD-based growth method uses commercial ZnO powder and methane as a reducing agent and in this way combines good controllability of the growth process with low production costs in a technically very simple growth unit, without any toxic compounds involved.⁵ In this work, we are reporting on the use of this novel growth method and the optimization of growth parameters for ZnO layer growth on Si substrates with an intermediate AlN nucleation layer. Because we achieved very good results for ZnO layer growth on a c-sapphire substrate, we transfer this empirical knowledge to the more challenging growth on a Si substrate.^{24,25}

EXPERIMENTAL SECTION

Prior to the growth experiments the natural amorphous SiO₂ layer was removed from the Si substrates by immersing the 2 in. Si wafers in peroxymonosulfuric acid (H₂SO₅), which was produced by mixing sulfuric acid (H₂SO₄) and hydrogen peroxide (H₂O₂) in a 1:1 ratio. The peroxymonosulfuric acid was heated to 120 °C, and the wafers were placed in it for 10 min and cleaned afterward with purified water. In the next step, the wafers were put in 2% hydrofluoric acid (HF) for 1 min and again cleaned afterward with purified water. Immediately after this, the Si substrates were overgrown with an AlN nucleation layer to cover the surface in order to prevent reoxidation. For the AlN nucleation layer growth a low-pressure horizontal flow MOVPE reactor (Aixtron Aix-200/4 RF-S) was used. The standard precursors trimethylaluminum (TMAI) and high-purity ammonia (NH₃) were used in a 1:3400 ratio. As the carrier gas, Pd-diffused hydrogen was used, while the reactor pressure was kept at 80 hPa. The growth temperature was controlled by a fiber-coupled pyrometer facing the back side of the rotation tray. In addition to this, the actual surface temperature of the samples was checked by a Laytec Epi-TT pyrometer device: the AlN nucleation layer growth temperatures mentioned below are the readout temperatures of this surface pyrometer. The nominal nucleation layer growth time refers to the time both TMAI and NH₃ were flowing into the reactor. In total, eight differently grown AlN nucleation layers were deposited on eight 2 in. Si(111) substrates. The wafers were cleaved into about 2 cm² pieces and finally overgrown with a ZnO layer. For the growth of the ZnO layers a methane (CH₄)-based CVD growth process was used as described by Huber et al.²³ The growth system consisted of a conventional three-zone furnace (Carbolite HZS 12/600) in

combination with a horizontal quartz glass liner tube, which was equipped with gas inlets for argon (99.998% purity), oxygen (99.999% purity), and a methane/argon mixture (1:9 ratio, 99.5% purity) on one end and held at a constant underpressure by a regulated vacuum pump connected to the other end. The gas flows were regulated by computer-controlled mass flow controllers (MFCs), while the vacuum pump ensured a constant pressure of 930 hPa in order to obtain a laminar gas flow. For the growth process commercially available ZnO powder (99.9% purity, Grillo Zinkweiss Pharma 8) was placed in the middle of the heating zone nearest to the gas inlets, which was heated to 940 °C. The main impurities within the ZnO source powder were Pb (<20 ppm), S and Cl (<10 ppm), and Fe, As, and Cd (<5 ppm); all other impurities were below 1 ppm. Most likely these impurities were not transferred to the substrate, as the use of a more pure source material did not affect the final crystal purity. Therefore, we obtained extremely low background doping concentrations for our ZnO layers, as previously reported.²⁵ A recent secondary ion mass spectrometry (SIMS) measurement on equivalent ZnO layers grown on a sapphire substrate confirmed the extremely low background doping concentration: namely, for the most common donors aluminum (2.2 × 10¹⁵ cm⁻³) and gallium (1.9 × 10¹⁴ cm⁻³) and the most common acceptors iron (1.8 × 10¹⁴ cm⁻³) and lithium (below the limit of detection, <1.5 × 10¹³ cm⁻³). The substrate was placed in the middle of the last heating zone, which was heated to 650 °C. For the middle heating zone the temperature was set to 780 °C. Due to cross-heating of the zones, the actually measured substrate temperature in the last heating zone was 720 °C in this configuration, which in the following is referred to as the growth temperature. Before the growth sequence was started, the tube was flushed with pure argon for 10 min to remove the ambient atmosphere. After this, the argon flow was reduced to 140 mL/min and 0.68 or 0.83 mL/min oxygen was added (optimized for the respective nucleation layers), while the liner tube was heated to the aforementioned temperature profile. When the desired temperature profile was reached, the actual growth process was started by adding 15.2 mL/min of the methane/argon mixture. The methane reduced the ZnO powder source material, and metallic zinc vapor was created by the chemical reaction given in eq 1, as reported by Steinfeld et al.²⁶ and Ebrahim et al.²⁷



The argon carrier gas flow transported the created zinc vapor to the location of the substrate, following the temperature gradient. At the spot of the substrate, the lower temperature led to a reoxidation of the zinc vapor by the oxygen present in the gas flow, forming the ZnO layer. Subsequently, the time interval for which methane was added to the tube will be referred to as growth time. After the methane was turned off, the temperatures were kept at their initial values for another 20 min before cooling to ensure all methane had reacted and the zinc vapor was completely reoxidized.

In the second part of this report, we study the influence of growth temperature, methane to oxygen ratio (i.e., the II/VI ratio), and growth time on the resulting ZnO layer quality. For this purpose the temperature in the substrate heating zone and the oxygen flow were adjusted and thus differ from the (optimum) values given above.

Both the initial AlN nucleation layers and the final ZnO layers grown were characterized by atomic force microscopy (AFM) measurements (Dimension 3100, Digital Instruments). Additionally, the surfaces as well as the layer thicknesses (in a view of a cleaved cross-section of the sample) were evaluated by a Zeiss Leo DSM982 scanning electron microscope (SEM). A Zeiss Leo 1550 SEM equipped with an Oxford Instruments INCA Crystal system was used for electron backscatter diffraction (EBSD) measurements. For high-resolution X-ray diffraction measurements a Bruker D8 diffractometer with Cu K α radiation was used. High-resolution TEM images were recorded using a CS-corrected FEI Titan 80-300 transmission electron microscope operated at 300 kV. To investigate the optical properties at room temperature, PL measurements were performed using a 320 nm solid-state laser with an output power of 20 mW for excitation. The emitted light was dispersed by a grating monochromator with a 25 cm focal length and 300 lines/mm grating and

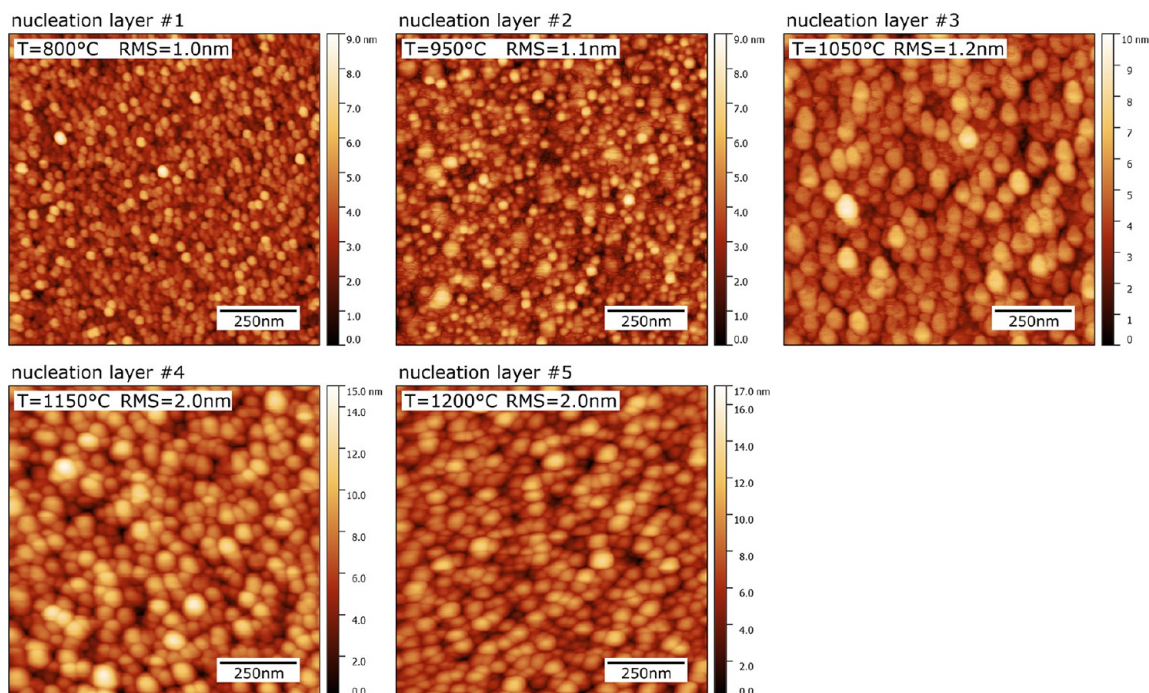


Figure 1. AFM micrographs of the AlN nucleation layers grown at different temperatures, before overgrowth with ZnO.

recorded by an UV-optimized liquid-nitrogen-cooled charge-coupled device camera (CCD). For low-temperature PL spectroscopy at 4.2 K, the same laser was used, but the sample was cooled in a liquid-helium-bath cryostat. In this setup the emitted light was analyzed by a grating monochromator with a 1 m focal length and 1200 lines/mm grating and also recorded with an UV-optimized liquid-nitrogen-cooled CCD.

RESULTS AND DISCUSSION

Influence of AlN Nucleation Layer Growth Temperature on ZnO Layer Quality. For the first series of five samples, we varied the AlN growth temperature between 800 and 1200 °C, while the rest of the parameters given above remained unchanged. In Figure 1 are presented AFM micrographs of the resulting nucleation layers. With increasing growth temperature the roughness of the AlN nucleation layer increases up to an RMS value of 2.0 nm for the two layers grown at highest temperatures (1150 and 1200 °C). Furthermore, the grain size is largest for the samples grown at 1050 and 1150 °C, as depicted in Figure 1.

As depicted in Figure 2, the AlN thickness decreases with increasing temperature; a similar decrease in AlN growth rate was theoretically predicted by Pu et al.²⁸ and confirmed experimentally by Chen et al.²⁹ Both observed a decrease in growth rate already above a growth temperature of ~500 °C at a reactor pressure of ~115 hPa and explained this by parasitic reactions occurring in the gas phase. Ho et al. observed a monotonic increase in AlN growth rate between 800 and 1100 °C, but for a reactor pressure below 1 hPa. Comparing these results with the results shown in Figure 2 and keeping in mind that the reactor pressure used here was 80 hPa, we conclude that parasitic reactions in the gas phase take place in our setup at growth temperatures above 950 °C and therefore lower the growth rate.

In order to evaluate the effect of the nucleation layer growth temperature, all of these nucleation layers were overgrown with a ZnO layer using the same growth parameters (i.e., pressure 930 hPa, growth temperature 720 °C, Ar 140 mL/min, O₂ 0.68

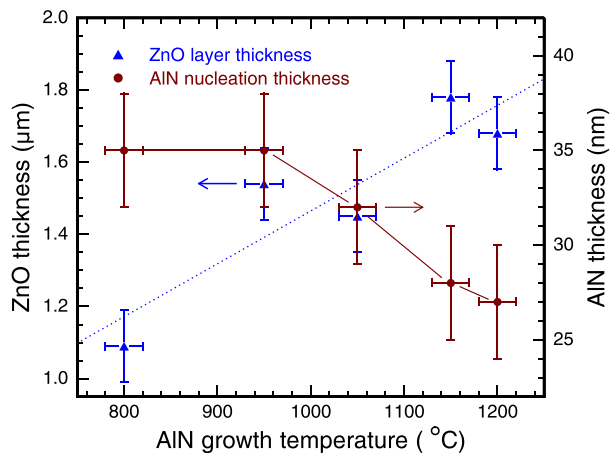


Figure 2. Dependence of the AlN nucleation layer and ZnO layer thickness on the AlN nucleation layer growth temperature. The ZnO layers were grown for 30 min.

mL/min, methane/argon mixture 15.2 mL/min, growth time 30 min). From Figure 2 we find that the ZnO layer thickness increases with increasing nucleation layer growth temperature: i.e., the ZnO growth rate correlates with the roughness of the nucleation layers.

In Figure 3, SEM images taken from the surface of the final ZnO layers are shown. Sample #1 shows a rather polycrystalline structure with a rough surface. For sample #2 the crystallites are larger in size in comparison to sample #1, but they still seem to be tilted and not well aligned. On comparison of samples #2 and #3, the crystallite sizes appear to be similar, but the surface of sample #3 is smoother and extended cracks are visible. On sample #4 the crystallites are not as clearly distinguishable as for the other samples, and the surface appears to be smoother than in the other cases, while the cracks are becoming wider. Sample #5 again shows more tilted and distinguishable crystallites with some holes in between.

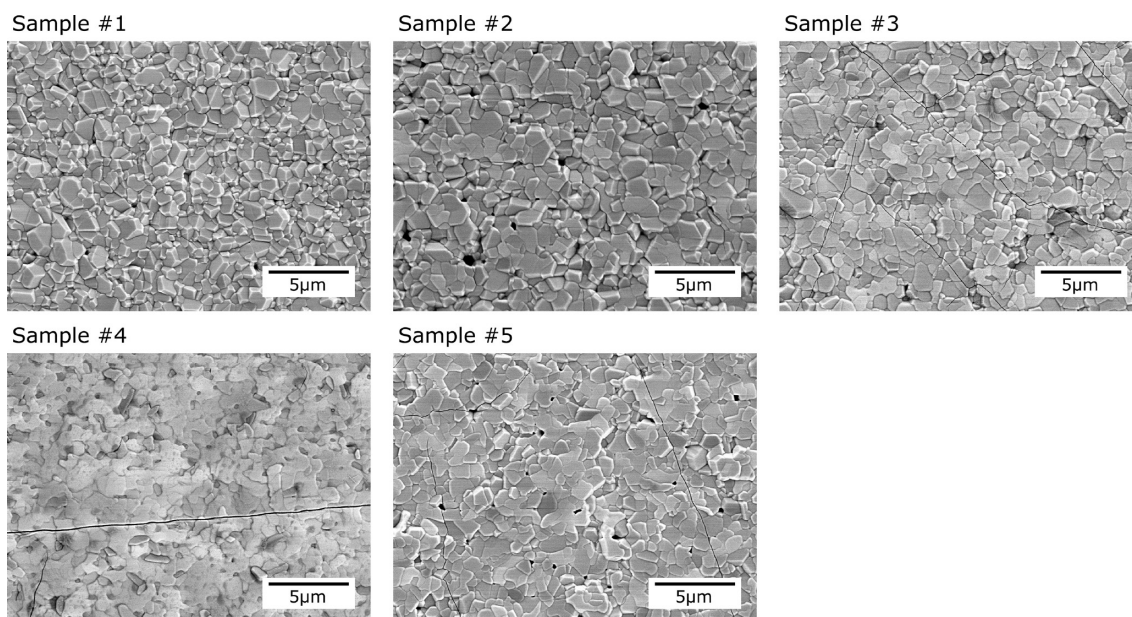


Figure 3. Top view SEM images of the ZnO layers grown on the different AlN nucleation layers shown in Figure 1. The AlN nucleation layers were grown at 800 °C (sample #1), 950 °C (sample #2), 1050 °C (sample #3), 1150 °C (sample #4), and 1200 °C (sample #5).

According to these images, an AlN nucleation growth temperature of 1150 °C is favorable for the growth of the ZnO layers.

To gain information about the orientation of the ZnO crystallites, EBSD measurements were performed. The inverse pole figures for the first five samples are shown in Figure 4. The results of these measurements support the findings from the SEM images. The ZnO layer of sample #1 is preferentially c-oriented, but with a large angular distribution around the [0001] direction. Furthermore, the crystallites in this sample are randomly rotated, as can be concluded from the rolling and transverse inverse pole figures. Obviously, there is no rigid epitaxial relation between the ZnO layer and the substrate. With increasing nucleation layer growth temperature, the c orientation is drastically improved, being best for sample #4 with a nucleation layer grown at 1150 °C, for which an almost perfect c orientation is observed. For sample #5 with a nucleation layer grown at even higher temperature (1200 °C), a broader distribution of crystal orientations is observed again, and the same holds for the rolling and transverse direction of the crystallites. For sample #4, heavily rotated domains are mostly absent.

Thus, the EBSD measurements prove that the best crystal alignment is achieved for an AlN nucleation layer grown at 1150 °C. This is also supported by the HRXRD ω scans shown in Figure 5. In this plot, the fwhm values of the ZnO (0002) and (10 $\bar{1}2$) reflections of an ω scan are given for all five samples as a function of the AlN nucleation layer growth temperature. The fwhm of the ZnO (0002) reflection decreases monotonically from 15.0° for the nucleation layer grown at 800 °C to 1.72° for the that grown at 1150 °C, respectively, and goes up again to 5.2° for the nucleation grown at an even hotter temperature (1200 °C). This improvement is even more clearly manifested in the (10 $\bar{1}2$) reflection. The (10 $\bar{1}2$) reflection for sample #1 was not measurable, thus indicating that the crystals are randomly rotated, which fits with the observations from EBSD measurements (see sample #1, rolling and transverse

directions, Figure 4). Sample #4 shows a fwhm value of 2.73° for the (10 $\bar{1}2$) reflection, which is much below the values of the other samples, meaning that this sample shows the best crystallite ordering in terms of rotational alignment—which again is in accord with the EBSD rolling and transverse direction data of this sample (Figure 4).

Figure 6 shows low-temperature ($T = 4.2$ K) PL spectra of the ZnO layers. All spectra are dominated by a donor-bound exciton emission D^0X of unknown origin in addition to a free exciton emission related to the A valence band $FX_A^{n=1}$ (ground state, $n = 1$).³⁰ Very likely, the peak associated with $FX_A^{n=1}$ in Figure 6 also partially contains emission of excitons bound to the surface, which cause a broad emission centered around 3.367 eV with a related low-energy tail.³¹ This explanation becomes obvious when the PL spectra (Figure 6) and the SEM images (Figure 3) are compared: sample #4 has the smoothest surface and shows no pronounced PL emission around 3.367 eV. This overlap of two emission processes is a reasonable explanation for the higher intensity of the peak assigned to the free exciton relative to the D^0X emission. Due to the large lattice mismatch and the different thermal expansion coefficients of the Si substrate and ZnO layer, the ZnO is heavily biaxially strained tensile, and therefore the D^0X emission is broadened and no sharp emission lines are visible. Therefore, a chemical identification of the donors is not possible. About 4.8 meV higher in energy relative to the free exciton emission $FX_A^{n=1}$, the weaker upper polariton branch (UPB_A) is observable.³² Furthermore, a free exciton emission related to the B valence band is observable ($FX_B^{n=1}$).³³ The (strain-dependent) splitting between the A and B valence bands found here is about 8.5 meV. Wagner et al. calculated 11.6 meV and measured 7.0 meV for this.³³ About 3 orders of magnitude lower in intensity and about 50 meV above the $n = 1$ ground state, the first excited state of the free exciton $FX_A^{n=2}$ is observable.³⁴ Other spectroscopic features such as a donor–acceptor pair (DAP) band at around 3.287 eV and the so-called structural defect related Y line at 3.332 eV are observed for most of the samples grown.^{32,35} At 3.31 eV emission from

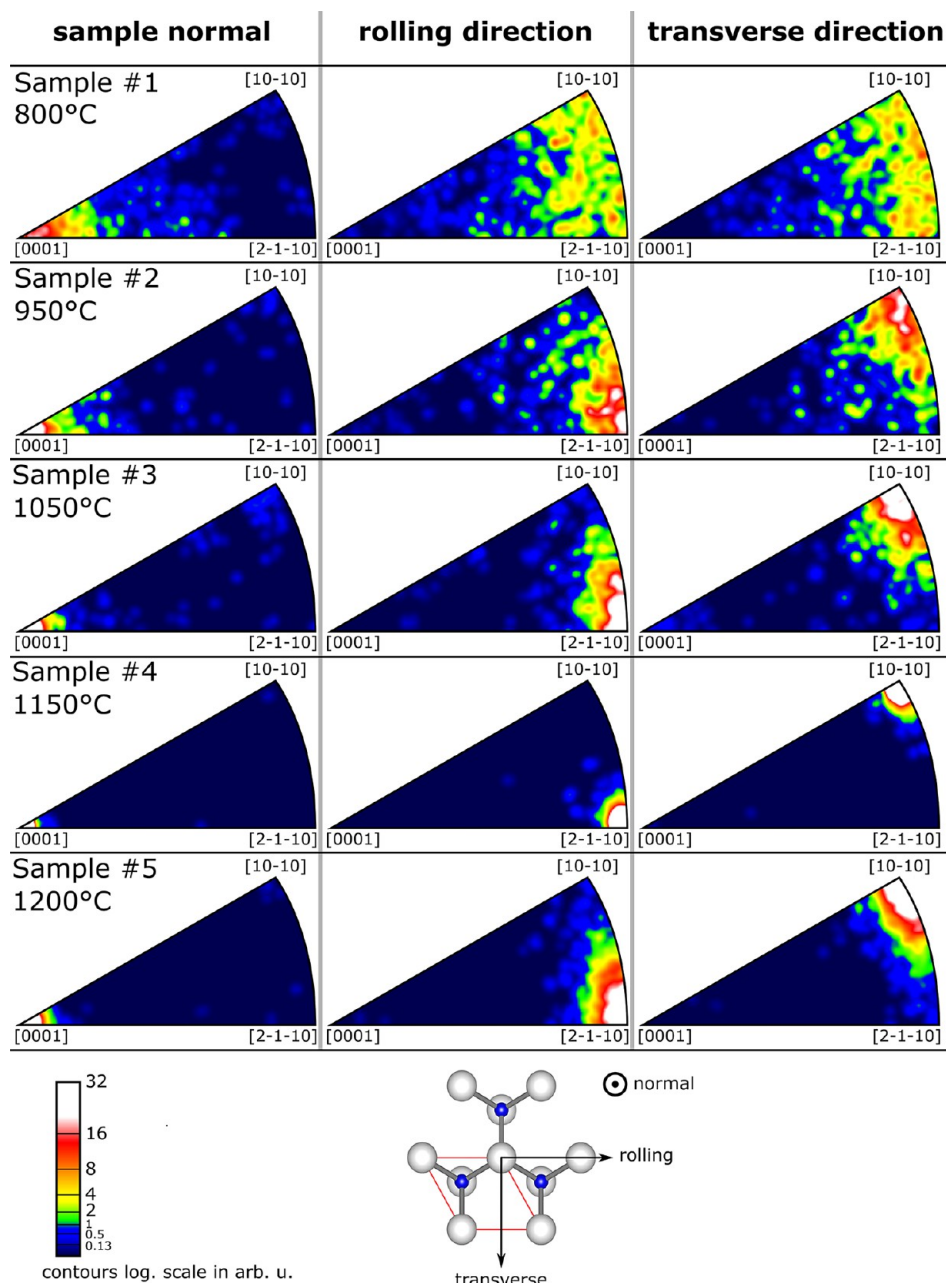


Figure 4. Inverse pole figures from EBSD measurements of the ZnO layers grown on different AlN nucleation layers.

basal plane stacking faults (BSF)³⁶ is visible for all samples except sample #4, confirming the higher crystal quality of the latter sample as discussed above. However, the near band edge emission around 3.36 eV is broadened for this sample, and it is not possible to distinguish the overlapping emissions. This broadening is most likely due to higher strain within the ZnO layer in comparison to the other samples. Along with the results discussed above, we conclude that the epitaxial connection is best for sample #4, hinting at the best crystal quality and crystalline orientation, but the epitaxial layer is subject to the largest strain.

Influence of AlN Nucleation Thickness on ZnO Layer Quality. In order to further improve the quality of the nucleation layer and therefore the ZnO layer, we used the optimized nucleation growth temperature of 1150 °C from the section above and then varied the growth time of the AlN nucleation layer between 10 and 20 min. As a result, the AFM

micrographs in Figure 7 show similar grain sizes and only slight differences in the roughness values of the three nucleation layers grown. In any event, from Figure 9 one can see a linear increase of the nucleation layer thickness from 30 to 40 nm with increasing growth time.

These nucleation layers again were overgrown with ZnO. The ZnO growth parameters used in the first section were optimized for those nucleation layers all grown for 10 min. When the same parameters were used to overgrow nucleation layers #7 (15 min) and #8 (20 min), no closed layer was formed. Therefore, we had to increase the oxygen flow from 0.68 to 0.83 mL/min (therefore, the complete set of ZnO growth parameters was pressure 930 hPa, growth temperature 720 °C, Ar 140 mL/min, O₂ 0.83 mL/min, methane/argon mixture 15.2 mL/min, growth time 30 min). For this reason the crystal quality of sample #6 (10 min) is slightly lower in comparison to sample #4 (first series, also 10 min), although

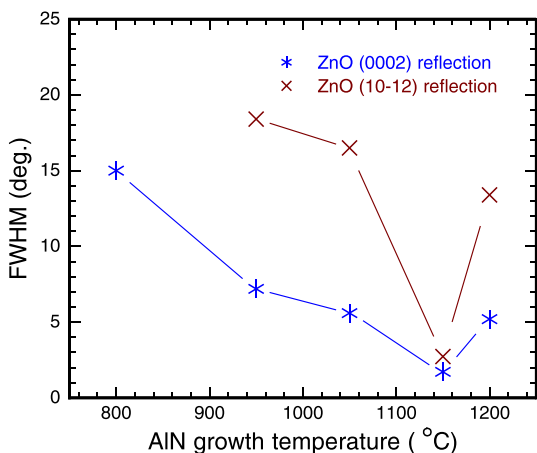


Figure 5. fwhm values of the HRXRD ω scans for the ZnO (0002) and (10 $\bar{1}2$) reflections as a function of the AlN nucleation layer growth temperature.

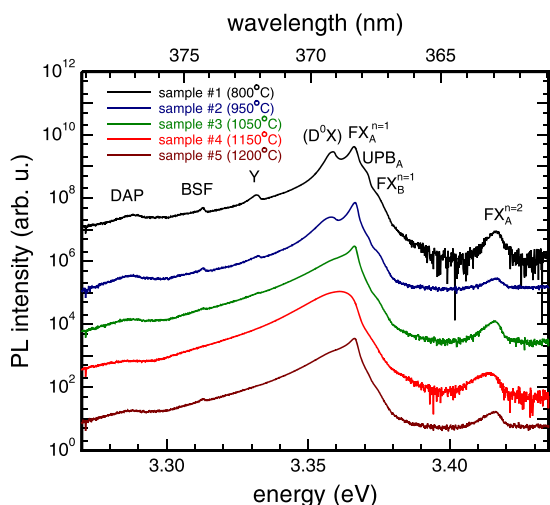


Figure 6. Low-temperature ($T = 4.2$ K) PL spectra of the ZnO layers grown on different AlN nucleation layers.

the nucleation layers are identical. A detailed study on the effect of the II/VI ratio in the gas phase on the ZnO growth will be given in the next section. SEM images and AFM micrographs of the nucleation layers overgrown with ZnO using the quoted parameters are shown in Figure 8. On the SEM images of all three samples, cracks in the ZnO layers with comparable densities are visible. A similar crack formation was reported previously in the literature for ZnO grown on Si(111)

by different methods such as PLD and MOVPE.^{18,37,38} Sample #7 shows a much smoother surface in the region between the cracks in comparison to the other two samples. This has been confirmed by AFM measurements shown in the second row of this figure (Figure 8). The RMS roughness value of sample #7 is measured to be 1.7 nm.

In Figure 9 (left) the ZnO layer thickness is plotted over the growth time of the nucleation layer. Interestingly, the ZnO layer grown on nucleation layer #7 (15 min) shows the lowest thickness. Seemingly, it is more difficult for the ZnO to attach to the nucleation crystallites of this nucleation layer in comparison to the other cases, although the roughnesses of all three nucleation layers are similar (see Figure 7). In the right graph of Figure 9 the fwhm values of ω scans of the ZnO (0002) and (10 $\bar{1}2$) reflections are given. Increasing the AlN nucleation growth duration from 10 to 15 min and therefore the AlN thickness from 30 to 35 nm decreases the resulting ZnO fwhm value drastically, down to values of 0.36 and 0.47° for the ZnO (0002) and (10 $\bar{1}2$) reflections, respectively. A further increase in the AlN growth duration and thus the AlN nucleation layer thickness to 40 nm does not lead to a further improvement of the ZnO fwhm value but drastically decreases the ZnO quality again (see Figure 9 (right)).

The related inverse pole figures of EBSD measurements are given in Figure 10. All three samples show an almost perfect c orientation along the sample surface normal: i.e., the ZnO crystallites are not tilted. Still, in the rolling and transverse directions, sample #6 (10 min) and sample #8 (20 min) show a distribution of orientations: i.e., the ZnO crystallites in these samples are rotated with a certain distribution. As indicated by the minimum bright spot size, the crystallites of sample #7 are perfectly aligned, confirming the findings from HRXRD measurements. It is remarkable that the thinnest ZnO layer (sample #7 (15 min); see Figure 7) leads to the best crystal quality in terms of HRXRD data, although an increasing layer thickness leads to a drastic improvement in ZnO crystal quality, as we will show in the following. Clearly, the improvement of the nucleation layer along with the AlN/ZnO interface leads to improved ZnO layer quality. For further insight, we performed HRTEM measurements on the AlN/ZnO interface of sample #7.

In Figure 11 a HRTEM image of the Si/AlN/ZnO interface is shown. Although the silicon substrate was cleaned and the silicon oxide was removed before AlN deposition as described, there is still an ~ 1.5 nm amorphous SiO_x or SiN_x layer on top of the Si substrate. SiO_x might be formed during the transfer in air for a few minutes between the cleaning process and MOVPE overgrowth, whereas SiN_x can be formed during the

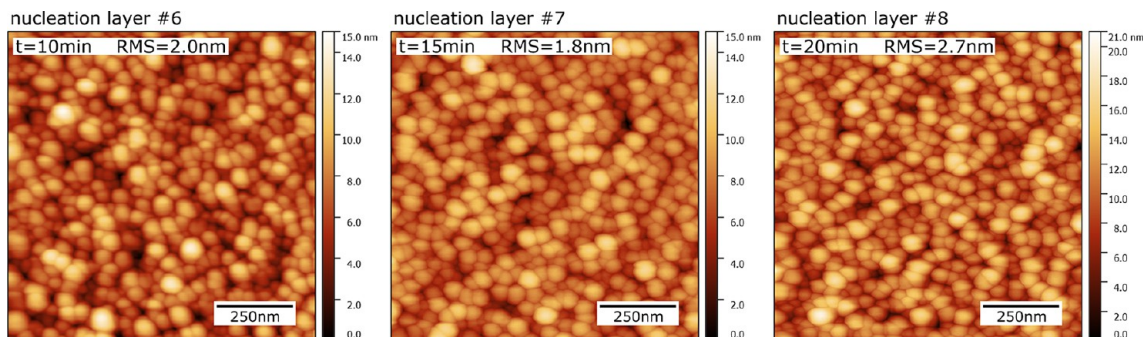


Figure 7. AFM micrographs of the AlN nucleation layers grown for different times before final overgrowth with ZnO.

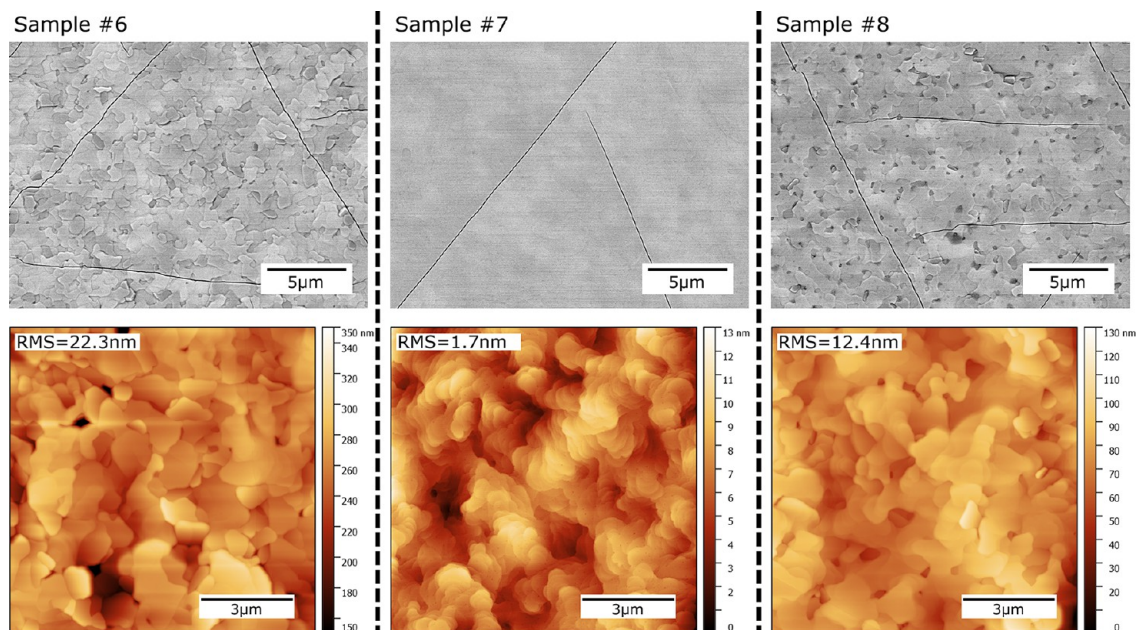


Figure 8. Top view SEM images (top) and AFM micrographs (bottom) of the ZnO layers grown on different AlN nucleation layers. Note the different height scales.

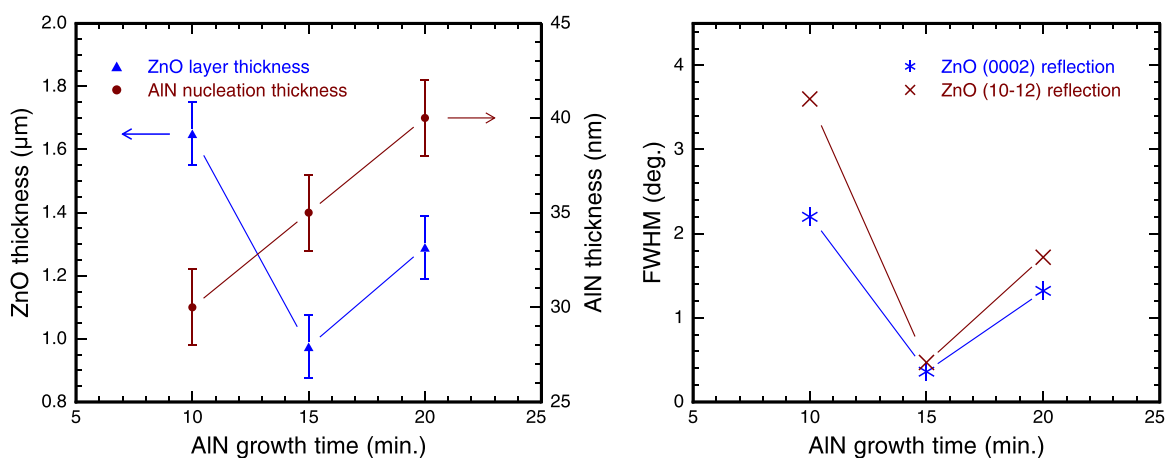


Figure 9. (left) AlN nucleation layer thickness and final ZnO layer thickness dependence on the AlN nucleation layer growth duration, as measured by SEM on a cleaved cross-section of the samples. (right) Dependence of the fwhm value of the HRXRD ω scans for the ZnO (0002) and (10 $\bar{1}2$) reflections on the AlN nucleation layer growth duration.

AlN nucleation layer growth. Unfortunately, we were not able to distinguish these two possibilities from the HRTEM images. The AlN thickness of 35 nm as measured by SEM (given in Figure 9, left) is confirmed by the TEM image as marked by the black bar. The surface of the AlN layer is not completely smooth but shows some hills with 5–7 nm height, which was already expected from the AFM micrograph given in Figure 7.

The AlN/ZnO interface was investigated in more detail by HRTEM (see Figure 12). A cross-section micrograph of this interface is given in Figure 12a). For Figure 12b this image was Fourier transformed and the (0001) peak eliminated before performing an inverse Fourier transformation, resulting in an image representing the basal planes both of AlN and ZnO. From this, the dislocations in the basal planes can clearly be seen. Both AlN and ZnO layers are extremely defect rich in this interface region, which is due to the large lattice mismatch to the silicon substrate. Figure 12c,d show the Fourier transformed images of the areas of the HRTEM image marked by

blue dashed lines: i.e., one of the ZnO and the other of AlN, respectively. In the FFT image of the latter area (Figure 12d), a stronger and also a weaker rotated pattern are observable, which both are introduced by tilted crystallites. Such tilted domains in the AlN nucleation were observed by us earlier in HRXRD for a similar AlN nucleation layer on sapphire instead of silicon.²⁴ In contrast, the ZnO FFT image shows no such rotated domains, from which we conclude that the ZnO basically forms a monocrystalline layer.

From the last two sections we conclude that there is an optimum temperature and thickness of the AlN nucleation layer for the subsequent ZnO layer growth. Li et al. concluded in their work on AlN nucleation on a sapphire substrate that the nucleation layer should not be too thick because a thick polycrystalline nucleation layer limits the quality of the following layer.³⁹ Similar behavior is observed here as well, as shown above. Nevertheless, in the case of ZnO growth on Si, the substrate must be fully covered in order to prevent

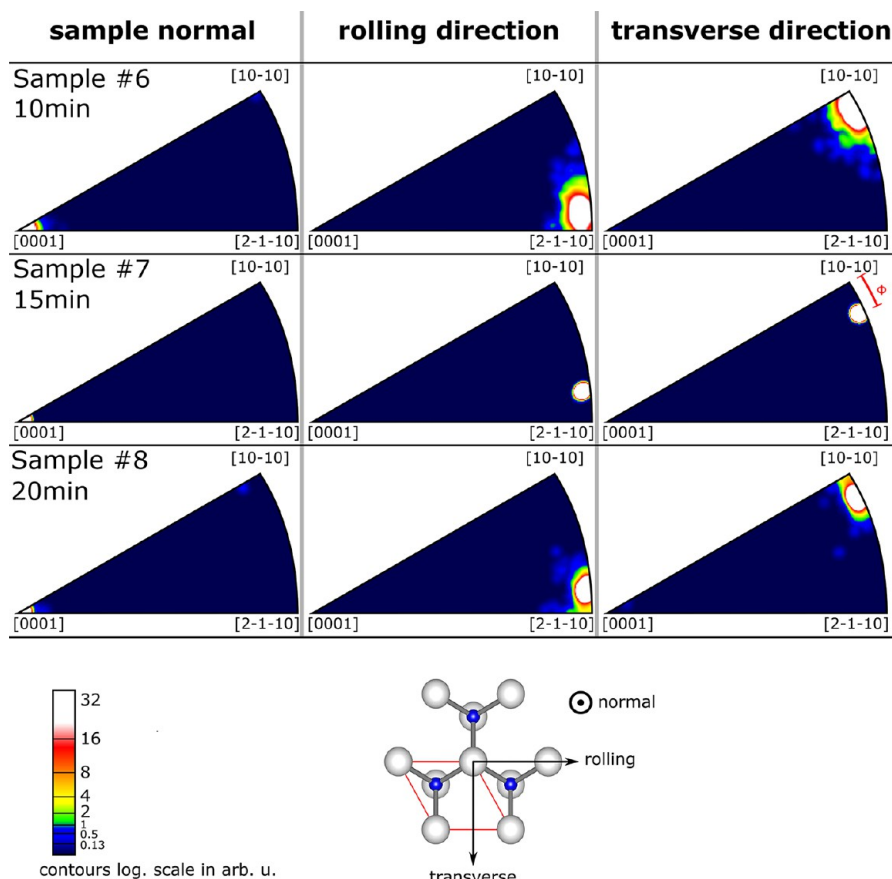


Figure 10. Inverse pole figures from EBSD measurements of the ZnO layers grown on AlN nucleation layers grown for different times (10/15/20 min).

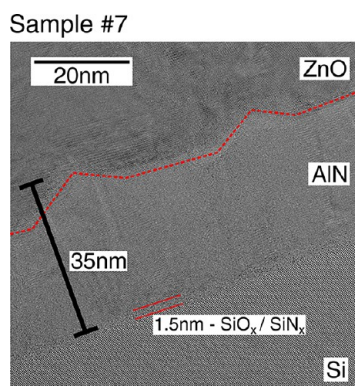


Figure 11. Cross-section HRTEM image of the Si/AlN/ZnO interface of sample #7. The dotted red line marks the AlN/ZnO interface.

oxidization of the Si surface, and so the nucleation layer should not be too thin. Gonsalves et al. reported on AlN nucleation layers for GaN growth on a sapphire substrate and found that a nucleation layer with bumps of suitable size is required to achieve good layer quality.⁴⁰ The same conclusion can be drawn here when the AFM images in Figure 1 are compared with the results obtained by overgrowth. So summing up this discussion, we find that the nucleation layer must provide a full coverage of the Si substrate but should not be too thick and bumps of suitable size are necessary.

Influence of CVD Growth Parameter Variation. For the optimization of ZnO layers the growth temperature was varied

for three different samples, without a change in the other growth parameters in comparison to the last section (pressure 930 hPa, Ar 140 mL/min, O₂ 0.83 mL/min, methane/argon mixture 15.2 mL/min, growth time 30 min). For all of the following samples an optimized nucleation layer grown for 15 min at 1150 °C is used. In Figure 13 SEM and AFM micrographs of these layers are given. The sample grown at 695 °C shows a closed layer with a few cracks (see Figure 13a), which most probably are formed during the cooling phase as a consequence of the difference in thermal expansion coefficients of the Si substrate and the ZnO layer (see Table 1), as discussed previously. The AFM micrographs of this sample (see Figure 13d,e) furthermore show a dense pattern of small holes mostly ordered along lines and distributed over the whole sample, resulting in a root-mean-square (RMS) value for the surface roughness of 3.6 nm. For a growth temperature of 720 °C, again a closed layer with the aforementioned cracks is formed (see Figure 13b). From the AFM micrographs of this sample (see Figure 13f) we found that the surface is completely closed and smooth, unlike the sample grown at lower temperature. The RMS roughness value of this specific sample is now reduced to 1.7 nm, which is remarkably low for ZnO grown on Si(111) substrate with an AlN nucleation layer in comparison to literature values. Wang et al.³⁷ reported a RMS value of 2.7 nm for an equivalent structure grown by MOVPE. A further increase in the growth temperature no longer leads to a closed layer but to wirelike columns as depicted in the SEM image in Figure 13c. For the sample grown at 695 °C, in HRXRD ω scans for the ZnO (0002) and

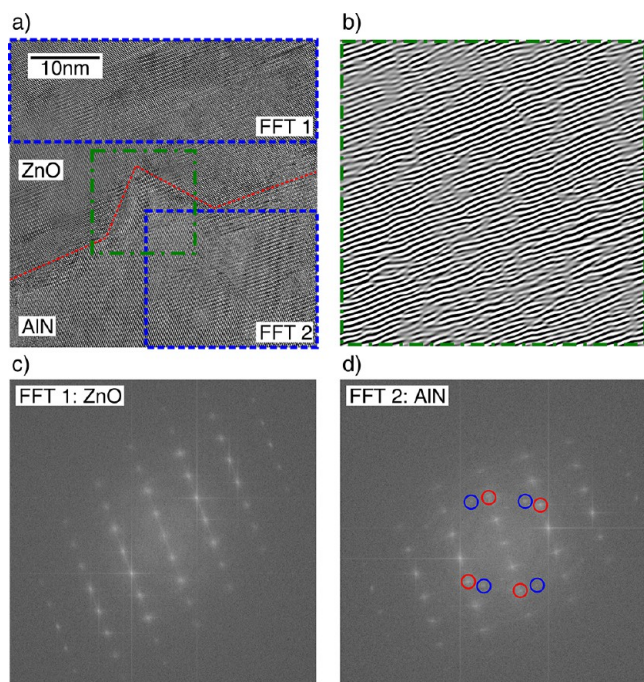


Figure 12. (a) Cross-section HRTEM image of the AlN/ZnO interface of sample #7. (b) c-plane ordering of the interface area marked in green in (a). (c) Fast Fourier transformed image of section labeled "FFT1" in (a), i.e. of the ZnO layer. (d) Fast Fourier transformed image of section labeled "FFT2" in (a) of the AlN nucleation layer.

($10\bar{1}2$) reflections fwhm values of 0.44 and 0.56° were measured, respectively. For the sample grown at 720°C these values were lower, reaching values of 0.36 and 0.48° , which confirms that for this temperature the crystalline quality and the surface roughness are superior, as discussed before.

In the next step the oxygen flow was varied in order to find the best CH_4/O_2 ratio (i.e., the best II/VI ratio), using again the optimized growth temperature of 720°C and keeping the other growth parameters unchanged. In Figure 14 SEM images of the resulting layers are shown. For the highest CH_4/O_2 ratio

of 2.24 no closed layer is formed but rather some columnar structure. For the two samples grown with CH_4/O_2 ratios of 2.00 and 1.83, respectively, closed layers are formed, looking almost identical from the SEM images (Figure 14b,c). When one looks at AFM micrographs of these two samples, shown in Figures 13f and 14f for the sample grown with a CH_4/O_2 ratio of 1.83 and for the sample with a CH_4/O_2 ratio of 2.00, respectively, a clear difference is obvious: the higher CH_4/O_2 ratio leads to a rougher surface (RMS value 7.2 nm) in comparison to the already mentioned RMS value of 1.7 nm for the sample grown with a CH_4/O_2 ratio of 1.83. A further decrease in the CH_4/O_2 ratio does not lead to a smooth surface but to a "fish-scale-like" structure as depicted in Figure 2d,e.

The results of HRXRD ω scans for the ZnO (0002) and ($10\bar{1}2$) reflections are shown in Figure 15 (left). For both scanning alignments a clear trend is observable, with the fwhm value being smallest for the sample grown with a CH_4/O_2 ratio of 1.83. When these HRXRD data are compared with the layer thickness of each sample as given in Figure 15 (right), an unexpected trend is observable: the sample grown with a CH_4/O_2 ratio of 1.83 and the lowest fwhm value of the ω scan (i.e., the best crystalline quality) is the thinnest sample. This is unexpected, because heteroepitaxial ZnO layers normally tend to show an improving crystalline quality with increasing thickness, as we will also show later in this report. From this we conclude that indeed the crystalline quality is largely influenced by changing the CH_4/O_2 ratio; thus, this result emphasizes the importance of a precise control of the II/VI ratio in ZnO layer growth. When the results from the HRXRD ω scans and the values for the surface roughness obtained in the AFM measurements are combined, it is clear that a growth temperature of 720°C and a CH_4/O_2 ratio of 1.83 leads to the best ZnO layers in terms of surface roughness and crystalline quality.

For all samples grown at different temperatures and with varying CH_4/O_2 ratios, low-temperature PL measurements were performed. The spectra obtained from these measurements are shown in Figure 16. For the samples grown at different temperatures (Figure 16, top) a clear difference

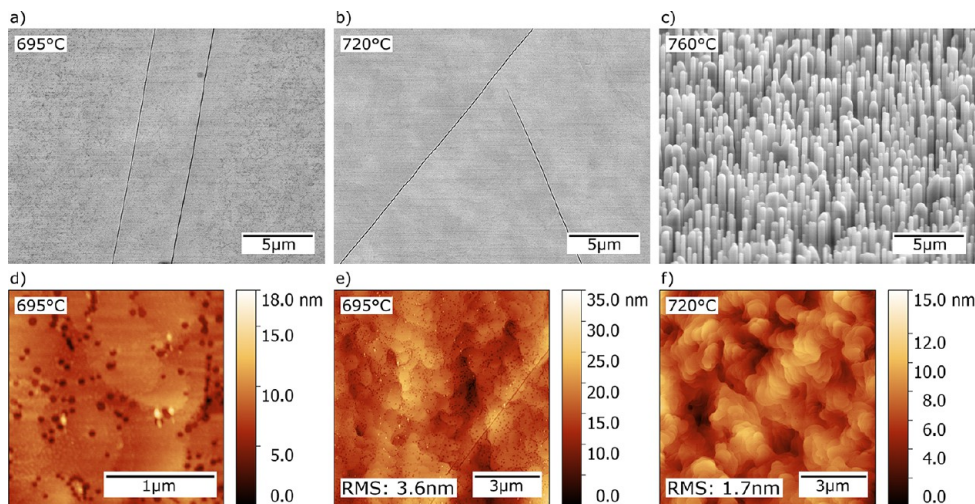


Figure 13. (a, b) Top view SEM images of the ZnO samples grown at different temperatures, as indicated in the insets. (c) SEM image of the sample grown at 760°C tilted by 60° . (d, e) AFM micrographs of the ZnO layer grown at 695°C with different magnifications. (f) AFM micrograph of the ZnO layer grown at 720°C and at a methane/oxygen ratio of 1.83.

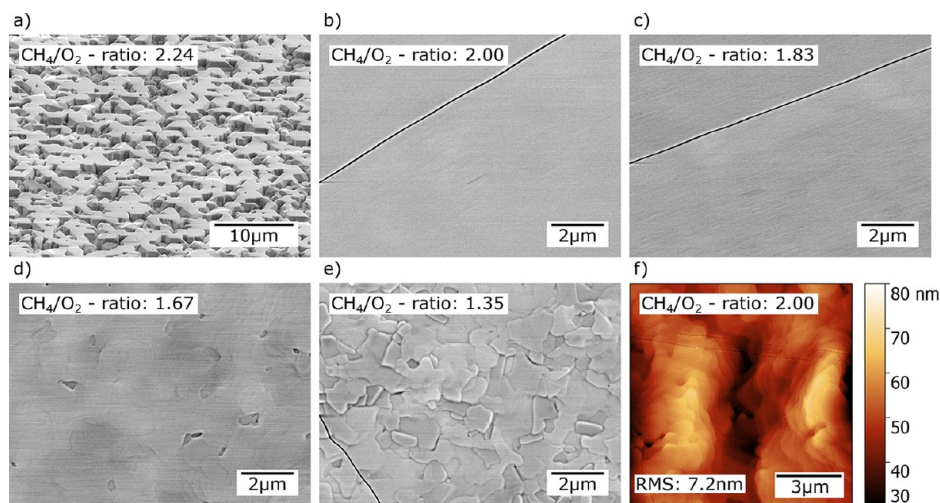


Figure 14. (a–e) Top view SEM images of the ZnO layers grown with different methane/oxygen ratios. (f) AFM micrograph of the ZnO layer grown at a methane/oxygen ratio of 2.0.

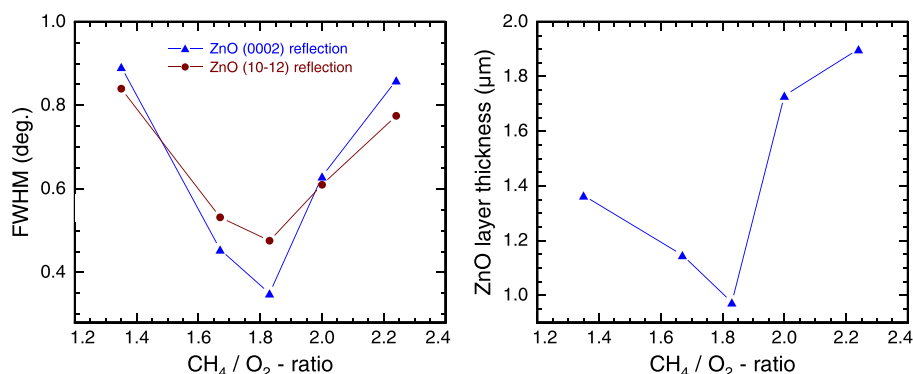


Figure 15. (left) fwhm values of the HRXRD ω scans for the ZnO (0002) and (10 $\bar{1}2$) reflections depending on the methane/oxygen ratio grown at 720 °C. (right) ZnO layer thickness dependence on the methane/oxygen ratio.

between the closed layers and the wirelike structure is observable. The spectrum of the sample grown at the highest temperature is dominated by sharp donor-bound exciton emission lines: namely, I_6 , which is assigned to aluminum, I_8 , which is assigned to gallium, I_{8a} , for which the chemical origin is still unknown, and I_9 , which is caused by excitons bound to indium donors.^{30,32} At this point it remains unclear whether this trace of impurities is coming from the source material or from the AlN nucleation layer grown in a MOVPE reactor mostly used for the growth of GaN. All of these impurities are commonly observed for layers grown with our setup, as reported previously.^{23,24} Furthermore, a broad emission of excitons bound to the surface (SX) centered at around 3.367 eV is observed.³¹ For the samples grown at lower temperatures, therefore forming closed layers, the spectra are very different. Only a single broad emission centered at around 3.365 eV is observable. Due to the large biaxial tensile strain caused by the large lattice mismatch between the Si substrate and ZnO, no distinguishable donor-bound emission lines are observable, and the center of the emission is shifted toward lower energy. Free exciton emission caused by a transition between the topmost conduction band and the A valence band $FX_A^{n=1}$ is observable on the high-energy shoulder of this broad bound exciton emission.³⁰ About 50 meV higher in energy, the emission from the first excited state of the free exciton $FX_A^{n=2}$ is observable, as also previously reported for similar heavily strained samples.¹⁷

For the samples grown with different CH₄/O₂ ratios the PL spectra are very similar, as shown in Figure 16 (bottom). As long as the layer is not closed and the ZnO is not heavily strained, sharp donor-bound exciton emission lines D⁰X and the so-called Y line at 3.332 eV related to structural defects are observable,³² as shown for the sample grown with a CH₄/O₂ ratio of 2.24. For the other samples with ratios from 2.0 to 1.35 the emission lines cannot no longer be separated, which is attributed to broadening by inhomogeneous strain. For all samples a weak contribution of a donor–acceptor pair (DAP) band at around 3.287 eV is observable.³⁵ At 3.31 eV emission from basal plane stacking faults (BSF)³⁶ is weakly observable for some of the samples, indicating a low density of such stacking faults.

Influence of ZnO Layer Thickness. In order to further increase the ZnO layer quality and to investigate the ZnO properties for increasing layer thickness, a series of samples was grown using the aforementioned optimized growth parameters (pressure 930 hPa, growth temperature 720 °C, Ar 140 mL/min, O₂ 0.83 mL/min, methane/argon mixture 15.2 mL/min) but now over different growth times varying from 10 min up to 240 min, resulting in layers with thicknesses between 0.67 and 2.54 μm as shown in Figure 17 (left). This figure shows a nonlinear increase of the ZnO layer thickness with growth time: i.e., the growth rate decreases over time. When the ZnO source material consumption over time plotted in the same

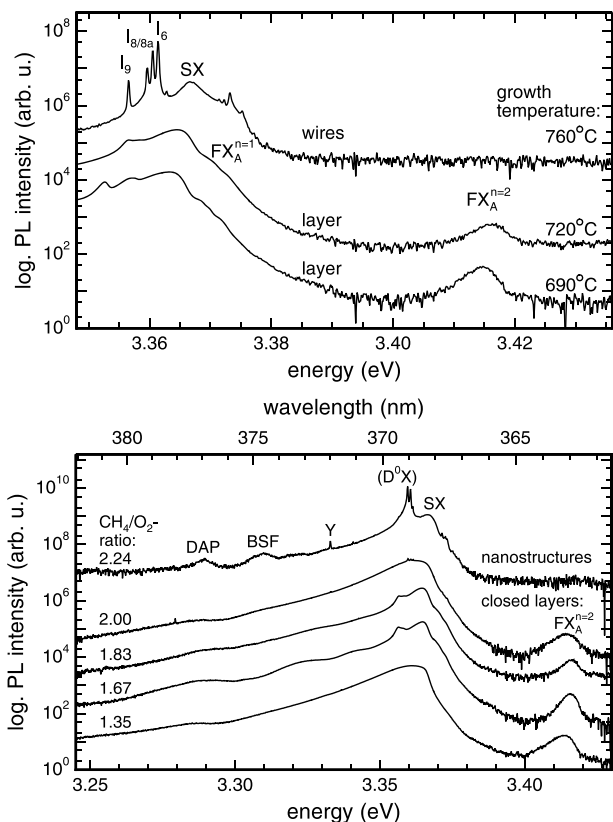


Figure 16. Low-temperature ($T = 4.2$ K) PL spectra: (top) samples grown at different temperatures with a methane/oxygen ratio of 1.83; (bottom) samples grown with different methane/oxygen ratios at 720 °C.

graph is taken into account, a good correlation between both is observed. From this finding we conclude that a decreasing zinc supply leads to a decrease in growth rate. The ZnO source material consumption shown here is the absolute weight loss of the ZnO powder source measured after each growth run. The graph on the right side of Figure 17 shows the fwhm values of HRXRD ω scans for the ZnO (0002) and (10 $\bar{1}$ 2) reflections plotted with respect to the layer thickness. Both values decrease monotonically for an increasing layer thicknesses, down to values of 712 and 1238 arcsec, respectively, for the ZnO layer with a thickness of 2.54 μ m. When these values are compared with the literature, to the best of our knowledge

Wang et al.³⁷ were the researchers reporting on a lower value for the (0002) reflection but a slightly higher value for the (10 $\bar{1}$ 2) reflection. They achieved values of 410 arcsec for (0002) and 1321 arcsec for the (10 $\bar{1}$ 2) reflection for MOVPE-grown 2.1 μ m thick ZnO layers, also on Si(111) with AlN buffer layer. For all these samples, except the one grown for 10 min, we measured the sample bowing radius by HRXRD as described by Liu et al.⁴¹ The sample grown for 10 min was not measurable, because for this growth time no closed layer was formed, as shown in Figure 20a. For the other samples a monotonic decrease of the sample bowing radius was measured, as shown in Figure 17 (right): i.e., with increasing layer thickness the sample curvature is higher. An explanation for this with a consideration of tensile stress within the ZnO layer will be given in the last section.

In order to measure the dislocation density, we performed HRXRD ω scans of the ZnO (0002) and (20 $\bar{2}$ 1) reflections, but this time with a smaller X-ray beam diameter reduced by a 0.3 mm pinhole. By constraint of the X-ray beam diameter, broadening of the fwhm due to sample bowing is suppressed. This is important for heavily curved samples, as shown above (see Figure 17 (right)), because the sample bowing would lead to an overestimation of the dislocation densities.⁴² Using the values obtained from these measurements, we calculated the dislocation density from the fwhm $\Delta\omega$ of the rocking curve according to the equations^{43,44}

$$\rho_{\text{screw}} = \frac{\Delta\omega_{0002}^2}{4.35 |\mathbf{b}_{\text{screw}}|^2} \quad \rho_{\text{edge}} = \frac{\Delta\omega_{20\bar{2}1}^2}{4.35 |\mathbf{b}_{\text{edge}}|^2} \quad (2)$$

where $\mathbf{b}_{\text{screw}} = [0001]$ and $\mathbf{b}_{\text{edge}} = 1/3[11\bar{2}0]$ denote the Burgers vectors of screw and edge dislocations, respectively. The obtained dislocation densities are plotted in Figure 18 (left) with respect to the layer thickness. We find that both screw and edge dislocation densities are decreasing for an increasing layer thicknesses, reaching values of $\rho_{\text{edge}} = 1.6 \times 10^{10} \text{ cm}^{-2}$ and $\rho_{\text{screw}} = 9.1 \times 10^8 \text{ cm}^{-2}$ for the thickest sample. Furthermore, we obtained the lateral coherence length (LCL) of the samples by performing a Williamson–Hall analysis. The required HRXRD ω scans of the ZnO (0002), (0004), and (0006) reflections were also carried out using the 0.3 mm pinhole in order to achieve reliable results. A detailed description of the Williamson–Hall analysis is given by Moram and Vickers.⁴⁴ The resulting values for the LCL are plotted in Figure 18 (right). When the value for the 1.9 μ m

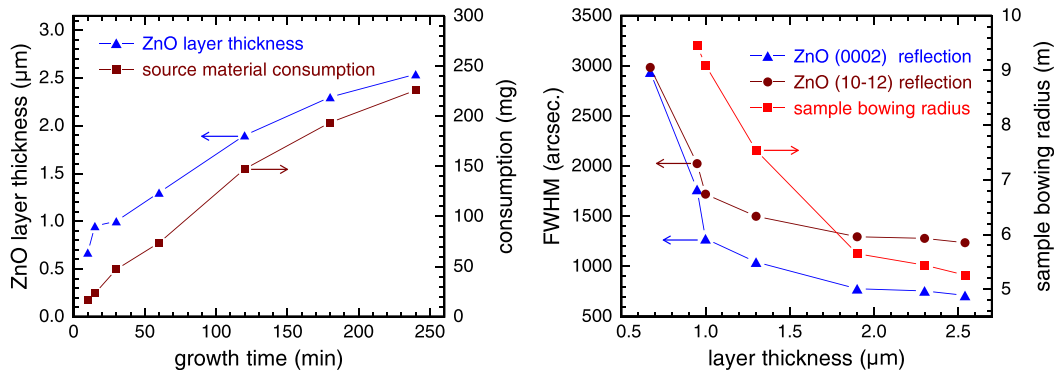


Figure 17. (left) ZnO layer thickness and ZnO source material consumption plotted over growth time for samples grown at 720 °C with a methane/oxygen ratio of 1.83. (right) fwhm values of the HRXRD ω scans for the ZnO (0002) and (10 $\bar{1}$ 2) reflections and sample bowing radius over ZnO layer thickness.

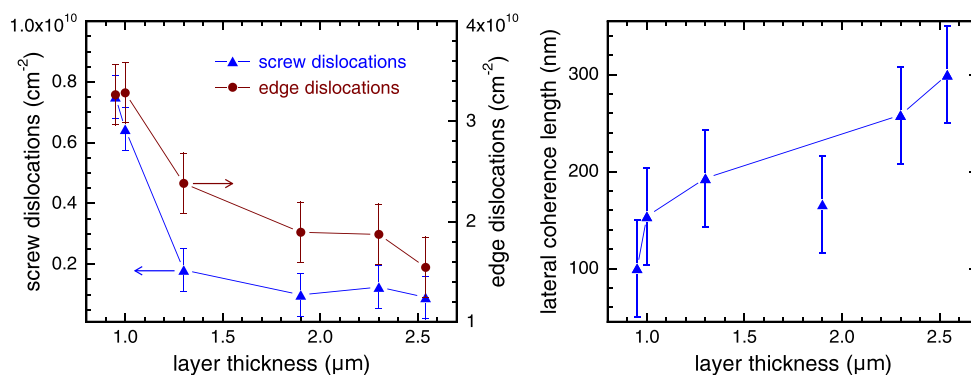


Figure 18. (left) Edge and screw dislocation densities calculated from the fwhm values of the HRXRD ω scans for the ZnO (0002) and (20 $\bar{2}$ 1) reflections, measured with a constricted X-ray beam diameter in order to reduce the influence of substrate bowing. For the edge and screw dislocation densities, errors of $\pm 3 \times 10^9$ and $\pm 7 \times 10^8$ cm⁻², respectively, were estimated. (right) Lateral coherence length over the layer thickness, as calculated from HRXRD data. For the LCL an error of ± 50 nm was estimated.

thick sample is neglected, a monotonic increase is observed for increasing layer thickness, reaching a value of $L_{\parallel} = 300$ nm. As the LCL is obtained by first fitting the ω -scan data and afterward using another fit for the Williamson–Hall plot,^{41,44} we estimate that an error of at least ± 50 nm has to be considered for the latter values.

To prove that an epitaxial relation between the Si(111) substrate and the ZnO layer is given, a combined ϕ scan of the Si {220} planes and the ZnO {1 $\bar{1}$ 02} planes was performed, as presented in Figure 19. This measurement shows that the ZnO

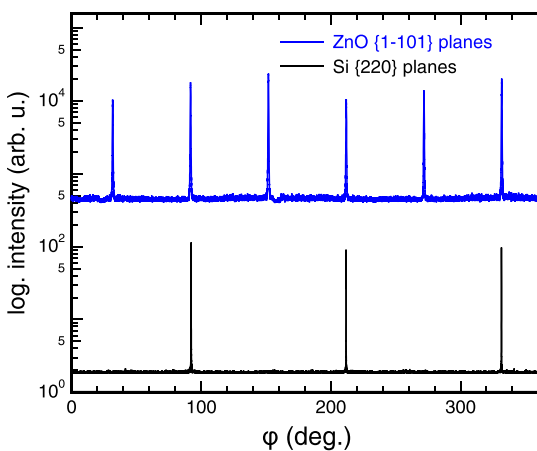


Figure 19. ϕ scan of the Si {220} planes and the ZnO {1 $\bar{1}$ 02} planes plotted on a logarithmic scale. For better visualization the ZnO scan is shifted upward.

m planes are perfectly parallel to the Si{220} planes; thus, the ZnO indeed aligns to the Si substrate despite the large lattice mismatch. In addition to this, the measurement also shows a perfect 6-fold symmetry of the ZnO crystal with no rotated domains present.

The improved layer quality with increasing layer thickness discussed above is also found for the surface roughness (see Figure 20). For the layer grown for 10 min a SEM top view image is shown in Figure 20a. This layer has a thickness of ~ 0.67 μm but is not fully closed. ZnO columns coalescing to a layer can be observed in this image, very similar to what we observed for the growth of ZnO on c-sapphire.²⁴ For a growth duration of only 15 min, a closed layer with a smooth surface (RMS = 2.7 nm) is formed, as evidenced by the AFM

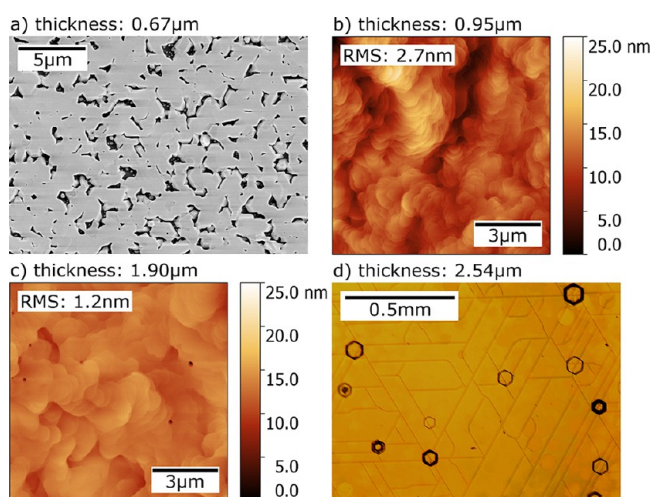


Figure 20. (a) SEM top view image of the sample grown for 10 min. (b) AFM micrograph of the sample grown for 15 min. (c) AFM micrograph of the sample grown for 120 min. (d) Microscope image of the sample grown for 240 min.

micrograph in Figure 20b. For a further increase in layer thickness the roughness approaches an RMS value of ~ 1 nm. The samples with a thickness larger than 1.9 μm show isolated small holes, as the AFM micrograph in Figure 20c proves. On the sample with a thickness of 2.5 μm (i.e., the thickest sample grown), microscopic hexagonal structures are observed on the surface (see Figure 20d). For all samples (except that grown for only 10 min) we find macroscopic cracks intersecting at $\sim 60^\circ$. We conclude that, as soon as a closed layer is formed, the thermal stress during the cooling phase after growth becomes too large, and for partial relaxation these cracks are formed. On the thickest layer macroscopic dark hexagonal structures occur mainly at the intersection of multiple cracks, as depicted in Figure 20d. A detailed study of these hexagonal structures is given in the Supporting Information.

In Figure 21 PL spectra of this series of samples are displayed. Figure 21 (top) shows the normalized low-temperature PL spectra of the near band edge emission, dominated by the free exciton emission $FX_A^{n=1}$, with its first excited state $FX_A^{n=2}$, and emission from excitons bound to surface defects (SX). Additionally, two details are observed for increasing layer thickness: first, the spectra shift toward higher energy, and second, the gallium-related donor-bound exciton

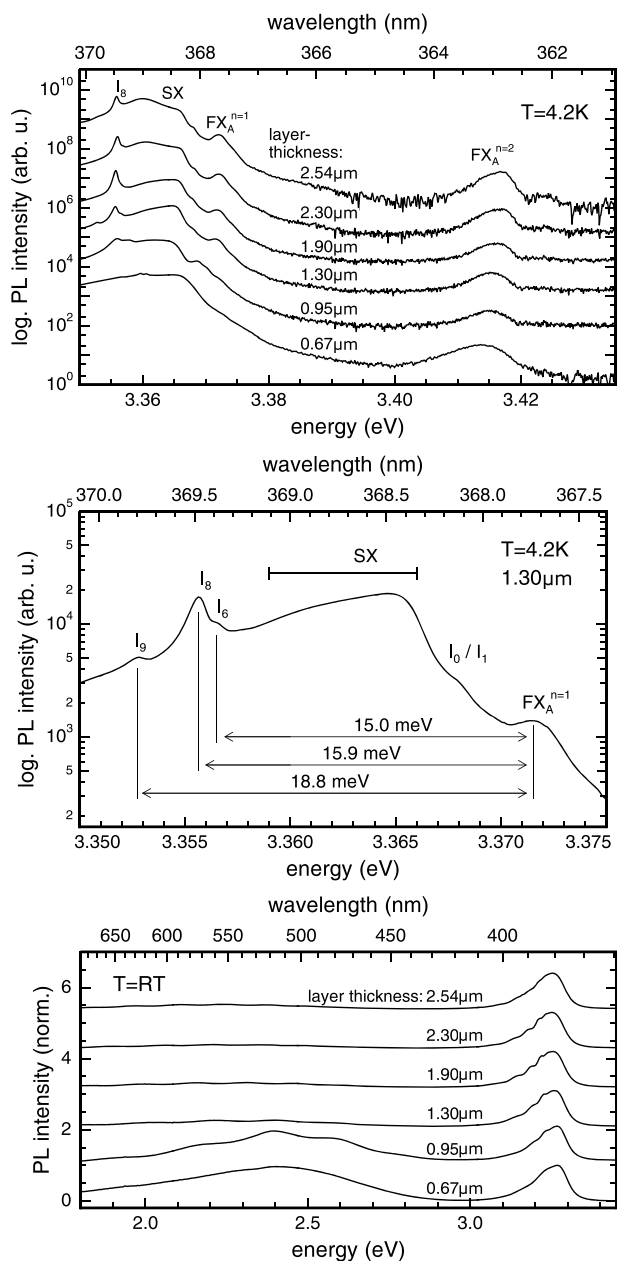


Figure 21. (top) Low-temperature ($T = 4.2$ K) PL spectra of the near band edge emission of ZnO for different layer thicknesses. (middle) Details of the excitonic emission region. (bottom) Room-temperature PL spectra of the defect-related emission at around 2.4 eV for different layer thicknesses, normalized to the near band edge emission.

(D^0X) emission peak I_8 emerges. We identify this peak actually located for this strained layer at $\sim 3.355_6$ eV by its spacing from $FX_A^{n=1}$, which is 15.9 meV and thus very close to the 16.1 meV quoted in the literature.³⁰ Also, the aluminum-related I_6 emission line is observed in this spectrum and again identified by its spacing of 15.0 meV from $FX_A^{n=1}$, matching the value of 15.1 meV given in the literature.³⁰ Lower in energy at 3.3527 eV, with a localization energy of about 18.8 meV (literature 19.2 meV³⁰), the indium-related I_9 peak can be identified. The deviation of the peak positions from the values given in the literature can be explained by strain and will be discussed in the next section, while the small deviation in localization energy can be explained by the broadening of the

peaks, especially of the $FX_A^{n=1}$ emission. In Figure 21 (bottom) room-temperature PL spectra normalized to the near band edge emission at 3.25 eV are given. For the layers with a thickness below 1 μm a pronounced green luminescence band centered at ~ 2.45 eV is observed, which vanishes for the thicker layers. The origin of this luminescence is still under debate in the literature. Studenikin and Cocivera suggest that donor–acceptor complexes, including an oxygen vacancy and a zinc vacancy, are causing this emission.⁴⁵ Egelhaaf and Oelkrug came to similar results,⁴⁶ while Xu et al. claimed that a transition from donor levels caused by zinc interstitials to deep acceptor levels from zinc vacancies causes the green luminescence.⁴⁷ Lin et al. assigned the green emission to transitions of electrons from the conduction band to oxygen antisite defect levels.⁴⁸ Whatever defects cause this emission, we can conclude that the underlying deep level defects vanish for increasing growth time, either because these defects anneal out during the ongoing growth or because the layer quality improves toward the surface with increasing thickness, because the PL signal is obtained from the topmost 100–200 nm only due to the limited penetration length of the exciting laser.

Biaxial Stress Analysis. As already mentioned, the lattice mismatch between the Si substrate and the ZnO layer and the difference in thermal expansion coefficients are quite large (see Table 1), and as a result the heteroepitaxial ZnO film must be heavily strained. In Figure 22 the stress depending on the ZnO

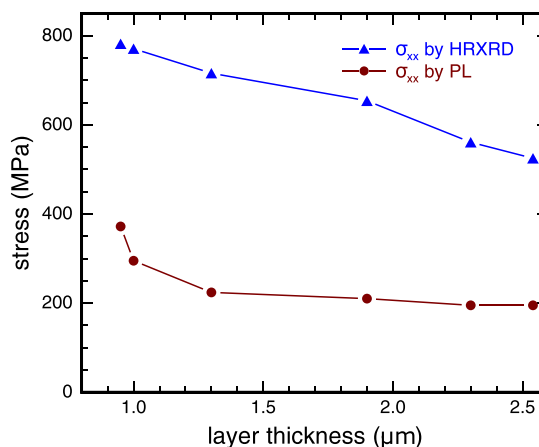


Figure 22. Biaxial stress depending on the layer thickness, derived from HRXRD measurements and from PL shifts.

layer thickness is given for the latter sample series, as calculated either from HRXRD measurements or from the shift of the free exciton $FX_A^{n=1}$ emission. The so-called Stoney formula (eq 3)^{49,50} was used to calculate the in-plane stress $\sigma_{xx(F)}$ in the ZnO film from the values of sample bowing radius (R) measured by HRXRD as given in Figure 17:

$$\sigma_{xx(F)} = \frac{E_S d_S^2}{6R(1 - \nu_S) d_F} \quad (3)$$

In this formula E_S is Young's modulus, ν_S the Poisson ratio, and d_S the thickness of the Si substrate, while d_F is the thickness of the ZnO film. The results of this calculation are given in Figure 22 and prove that the average stress in the ZnO layer decreases monotonically with increasing thickness. Obviously, the macroscopic cracks mentioned above (Figure 20d) lead to a relaxation of the ZnO layer. In the color plot, where the layer stress is plotted with respect to sample bowing

radius and ZnO layer thickness (Figure 23), the sample bowing radius is decreasing slowly with increasing ZnO layer thickness, leading to lower stress.

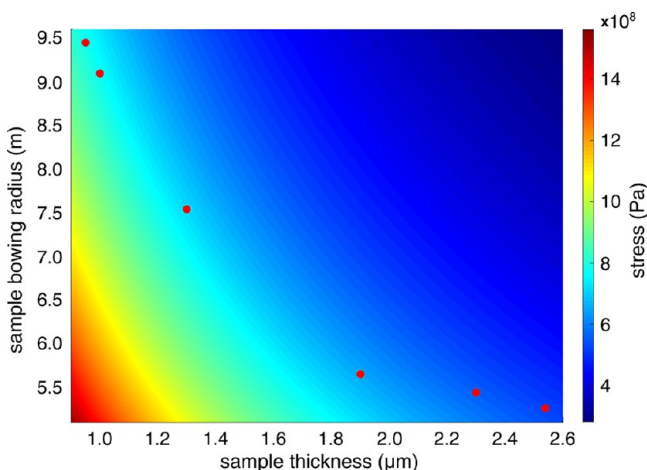


Figure 23. Biaxial stress measured by HRXRD depending on the sample thickness and the sample bowing radius.

To prove this, the stress within the upper part of the ZnO layer was additionally evaluated from the low-temperature PL measurements, using eqs 4–6. The deformation potentials D_i used in eq 4 are given in Table 2. The crystal-field and spin–

Table 2. Values Used for the Calculation of Layer Stress from PL Data

E_A^0	3.3759 eV ³⁰
E_C^0	3.4419 eV ⁵⁵
D_1	−3.90 eV ⁵⁶
D_2	−4.13 eV ⁵⁶
D_3	−1.15 eV ⁵⁶
D_4	−1.22 eV ⁵⁶
Δ_1	38.3 eV ⁵⁵
Δ_2	2.1 eV ⁵⁵

orbit splitting parameters Δ_1 and Δ_2 used in eq 5 are given in Table 2 as well. Thus, the equation

$$E(\text{FX}_A) = E_A^0 + (D_1 + D_2/\nu_F)\epsilon_{zz} + a_4(D_3 + D_4/\nu_F)\epsilon_{zz} - a_4 a_{-1} [(D_1 + D_2/\nu_F)\epsilon_{zz}]^2 (E_C^0 + E_A^0)^{-1} \quad (4)$$

using

$$2a_{\pm} = 1 \pm (\Delta_1 - \Delta_2) [(\Delta_1 - \Delta_2)^2 + 8\Delta_2^2]^{-1/2} \quad (5)$$

was solved for ϵ_{zz} .⁵⁵

Finally, eq 6 was used to calculate the strain within the basal plane.⁵⁷ The results of both methods are given in Figure 22. Although the absolute values for the layer stress calculated from PL are lower than the values deduced from HRXRD, both calculations yield decreasing stress with increasing layer thickness. When it is taken into account that ZnO has an absorption coefficient of $\sim 2 \times 10^{-5} \text{ cm}^{-1}$ for the laser wavelength of 320 nm used for excitation in the PL measurements, the laser is absorbed within the first $\sim 100 \text{ nm}$ ($I/I_0 = e^{-2}$);⁵⁸ thus, the measured PL spectra provide information only from the topmost region of the ZnO layer, while in HRXRD an average value for the whole layer is

measured. This supports the conclusion that the stress is decreasing within the ZnO layer toward the top.

$$\sigma_{xx} = -\frac{1}{\nu_F} E_F \epsilon_{zz} \quad (6)$$

SUMMARY

In summary, we present a study on the optimization of heteroepitaxial ZnO layer growth on Si(111) substrates with an intermediate AlN nucleation layer. The large effect of the AlN nucleation layer growth parameters on the final ZnO layer was demonstrated. The results indicate that an AlN nucleation layer grown by MOVPE at 1150 °C with a thickness of $\sim 35 \text{ nm}$ provides the best basis for overgrowth with a ZnO layer using a new CVD-based method with methane as a reducing agent of the ZnO powder source material. For nucleation layers grown at temperatures above or below 1150 °C we find a drastic increase in the fwhm of HRXRD ω scans for the final ZnO layer, which is also observed for thicker or thinner AlN nucleation layers. Furthermore, we optimized the growth parameters for the CVD ZnO growth. We found that the best layer quality is achieved with a growth temperature of 720 °C and a CH_4/O_2 ratio of 1.83. Smooth layers with an RMS roughness value of 1.2 nm and fwhm values of HRXRD ω scans of 710 and 1240 arcsec for the (0002) and (10 $\bar{1}$ 2) reflections, respectively, were achieved. An LCL value of $L_{\parallel} = 300 \text{ nm}$ and dislocation densities of $\rho_{\text{edge}} = 1.6 \times 10^{10}$ and $\rho_{\text{screw}} = 9.1 \times 10^8 \text{ cm}^{-2}$ were found for the best layer. Room-temperature PL studies show a decreasing defect density with increasing ZnO layer thickness, consistent with the measured dislocation densities. Low-temperature PL measurements prove that the main impurities in the layer are indium, gallium, and aluminum, and line positions were used to study the stress evolution within the layers dependent on the layer thickness. Additionally, the stress within the layers was measured by HRXRD, and it was confirmed that the biaxial stress decreases with increasing ZnO layer thickness. Obviously, the formation of macroscopic cracks leads to partial relaxation of the layers with increasing thickness. These macroscopic cracks appear on all samples, showing an epitaxial relation between the ZnO layer and the Si substrate. The reduction of the layer stress and therefore the density of these cracks has to be investigated further. In any event the good controllability of the growth method described here in combination with a cheap substrate and the good resulting layer quality makes this combined growth process a potential candidate for large-scale industrial applications.

ASSOCIATED CONTENT

Supporting Information

The Supporting Information is available free of charge at <https://pubs.acs.org/doi/10.1021/acs.cgd.0c00907>.

Detailed AFM and cathodoluminescence (CL) study on the macroscopic hexagonal structures on top of the layers (PDF)

AUTHOR INFORMATION

Corresponding Author

Raphael Müller – Institute of Quantum Matter/Semiconductor Physics Group, Ulm University, Ulm, Germany; orcid.org/0000-0002-9351-3643; Phone: +49 (0)731 50 26101;

Email: raphael.mueller@uni-ulm.de; Fax: +49 (0)731 50 26108

Authors

Okan Gelme – Institute of Quantum Matter/Semiconductor Physics Group, Ulm University, Ulm, Germany

Jan-Patrick Scholz – Institute of Functional Nanosystems, Ulm University, Ulm, Germany

Florian Huber – Institute of Quantum Matter/Semiconductor Physics Group, Ulm University, Ulm, Germany

Manuel Mundsinger – Central Facility for Electron Microscopy, Ulm University, Ulm, Germany

Yueliang Li – Central Facility for Electron Microscopy, Ulm University, Ulm, Germany

Manfred Madel – Institute of Quantum Matter/Semiconductor Physics Group, Ulm University, Ulm, Germany

Alexander Minkow – Institute of Functional Nanosystems, Ulm University, Ulm, Germany

Ute Kaiser – Central Facility for Electron Microscopy, Ulm University, Ulm, Germany

Ulrich Herr – Institute of Functional Nanosystems, Ulm University, Ulm, Germany

Klaus Thonke – Institute of Quantum Matter/Semiconductor Physics Group, Ulm University, Ulm, Germany

Complete contact information is available at: <https://pubs.acs.org/10.1021/acs.cgd.0c00907>

Notes

The authors declare no competing financial interest.

ACKNOWLEDGMENTS

The authors thank M. Hocker and M. Mangold for supporting the CL and PL measurements and Probion Analysis (Bagneux, France) for SIMS investigations. Furthermore, we thank F. Scholz for helpful discussions and providing the MOVPE equipment. This research was funded by the Deutsche Forschungsgemeinschaft (DFG) under project number 339461538.

REFERENCES

- (1) Janotti, A.; Van de Walle, C. G. Fundamentals of zinc oxide as a semiconductor. *Rep. Prog. Phys.* **2009**, *72*, 126501.
- (2) Janotti, A.; Van de Walle, C. G. Native point defects in ZnO. *Phys. Rev. B: Condens. Matter Mater. Phys.* **2007**, *76*, 165202.
- (3) Lyons, J. L.; Janotti, A.; Van de Walle, C. G. Why nitrogen cannot lead to p-type conductivity in ZnO. *Appl. Phys. Lett.* **2009**, *95*, 252105.
- (4) Park, C. H.; Zhang, S. B.; Wei, S.-H. Origin of p-type doping difficulty in ZnO: The impurity perspective. *Phys. Rev. B: Condens. Matter Mater. Phys.* **2002**, *66*, 073202.
- (5) Huber, F.; Riegert, S.; Madel, M.; Thonke, K. H_2S sensing in the ppb regime with zinc oxide nanowires. *Sens. Actuators, B* **2017**, *239*, 358–363.
- (6) Jung, J.-P.; Lee, J.-B.; Kim, J.-S.; Park, J.-S. Fabrication and characterization of high frequency SAW device with IDT/ZnO/AlN/Si configuration: role of AlN buffer. *Thin Solid Films* **2004**, *447–448*, 605–609.
- (7) Oh, M.-S.; Nirmala, R.; Navamathavan, R. Improved Structural and Electrical Properties of ZnO-Based Thin Film Transistors by Using Pulsed KrF Excimer Laser Irradiation. *J. Electron. Mater.* **2019**, *48*, 3137–3144.
- (8) Jang, J. S.; Kim, J.; Ghorpade, U.; Shin, H. H.; Gang, M. G.; Park, S. D.; Kim, H.-J.; Lee, D. S.; Kim, J. H. Comparison study of ZnO-based quaternary TCO materials for photovoltaic application. *J. Alloys Compd.* **2019**, *793*, 499–504.

(9) Liu, W.-R.; Li, Y.-H.; Hsieh, W. F.; Hsu, C.-H.; Lee, W. C.; Lee, Y. J.; Hong, M.; Kwo, J. Domain Matching Epitaxial Growth of High-Quality ZnO Film Using a Y_2O_3 Buffer Layer on Si (111). *Cryst. Growth Des.* **2009**, *9*, 239–242.

(10) Fujita, M.; Kawamoto, N.; Tatsumi, T.; Yamagishi, K.; Horikoshi, Y. Molecular Beam Epitaxial Growth of ZnO on Si Substrate Using Ozone as an Oxygen Source. *Jpn. J. Appl. Phys.* **2003**, *42*, 67–70.

(11) Fu, Z.; Lin, B.; Liao, G.; Wu, Z. The effect of Zn buffer layer on growth and luminescence of ZnO films deposited on Si substrates. *J. Cryst. Growth* **1998**, *193*, 316–321.

(12) Kawamoto, N.; Fujita, M.; Tatsumi, T.; Horikoshi, Y. Growth of ZnO on Si Substrate by Plasma-Assisted Molecular Beam Epitaxy. *Jpn. J. Appl. Phys.* **2003**, *42*, 7209–7212.

(13) Chen, Y.; Jiang, F.; Wang, L.; Zheng, C.; Dai, J.; Pu, Y.; Fang, W. Structural and luminescent properties of ZnO epitaxial film grown on Si(111) substrate by atmospheric-pressure MOCVD. *J. Cryst. Growth* **2005**, *275*, 486–491.

(14) Yoo, Y.-Z.; Sekiguchi, T.; Chikyow, T.; Kawasaki, M.; Onuma, T.; Chichibu, S. F.; Song, J. H.; Koinuma, H. V. defects of ZnO thin films grown on Si as an ultraviolet optical path. *Appl. Phys. Lett.* **2004**, *84*, 502–504.

(15) Fujita, M.; Kawamoto, N.; Sasajima, M.; Horikoshi, Y. Molecular beam epitaxy growth of ZnO using initial Zn layer and MgO buffer layer on Si(111) substrates. *J. Vac. Sci. Technol., B: Microelectron. Process. Phenom.* **2004**, *22*, 1484–1486.

(16) Gan, X.-W.; Wang, T.; Wu, H.; Liu, C. ZnO deposited on Si (111) with Al_2O_3 buffer layer by atomic layer deposition. *Vacuum* **2014**, *107*, 120–123.

(17) Guo, W.; Allenic, A.; Chen, Y. B.; Pan, X. Q.; Tian, W.; Adamo, C.; Schlom, D. G. ZnO epitaxy on (111) Si using epitaxial Lu_2O_3 buffer layers. *Appl. Phys. Lett.* **2008**, *92*, 072101.

(18) Lin, B. H.; Liu, W. R.; Yang, S.; Kuo, C. C.; Hsu, C.-H.; Hsieh, W. F.; Lee, W. C.; Lee, Y. J.; Hong, M.; Kwo, J. The Growth of an Epitaxial ZnO Film on Si(111) with a $Gd_2O_3(Ga_2O_3)$ Buffer Layer. *Cryst. Growth Des.* **2011**, *11*, 2846–2851.

(19) Kyun Lee, S.; Yeog Son, J. Epitaxial growth of thin films and nanodots of ZnO on Si(111) by pulsed laser deposition. *Appl. Phys. Lett.* **2012**, *100*, 132109.

(20) Tiwari, A.; Park, M.; Jin, C.; Wang, H.; Kumar, D.; Narayan, J. Epitaxial growth of ZnO films on Si(111). *J. Mater. Res.* **2002**, *17*, 2480–2483.

(21) Nahhas, A.; Kim, H. K.; Blachere, J. Epitaxial growth of ZnO films on Si substrates using an epitaxial GaN buffer. *Appl. Phys. Lett.* **2001**, *78*, 1511–1513.

(22) Jiang, F.; Zheng, C.; Wang, L.; Fang, W.; Pu, Y.; Dai, J. The growth and properties of ZnO film on Si(111) substrate with an AlN buffer by AP-MOCVD. *J. Lumin.* **2007**, *122–123*, 905–907.

(23) Huber, F.; Madel, M.; Reiser, A.; Bauer, S.; Thonke, K. New CVD-based method for the growth of high-quality crystalline zinc oxide layers. *J. Cryst. Growth* **2016**, *445*, 58–62.

(24) Müller, R.; Huber, F.; Gelme, O.; Madel, M.; Scholz, J.-P.; Minkow, A.; Herr, U.; Thonke, K. Chemical Vapor Deposition Growth of Zinc Oxide on Sapphire with Methane: Initial Crystal Formation Process. *Cryst. Growth Des.* **2019**, *19*, 4964–4969.

(25) Müller, R.; Huber, F.; Töws, M.; Mangold, M.; Madel, M.; Scholz, J.-P.; Minkow, A.; Herr, U.; Thonke, K. High-Quality ZnO Layers Grown by CVD on Sapphire Substrates with an AlN Nucleation Layer. *Cryst. Growth Des.* **2020**, *20*, 3918–3926.

(26) Steinfeld, A.; Brack, M.; Meier, A.; Weidenkaff, A.; Wuillemin, D. A solar chemical reactor for co-production of zinc and synthesis gas. *Energy* **1998**, *23*, 803–814.

(27) Ale Ebrahim, H.; Jamshidi, E. Kinetic Study of Zinc Oxide Reduction by Methane. *Chem. Eng. Res. Des.* **2001**, *79*, 62–70.

(28) Pu, K.; Dai, X.; Miao, D.; Wu, S.; Zhao, T.; Hao, Y. A kinetics model for MOCVD deposition of AlN film based on Grove theory. *J. Cryst. Growth* **2017**, *478*, 42–46.

(29) Chen, C.; Liu, H.; Steigerwald, D.; Imler, W.; Kuo, C.; Craford, M.; Ludowise, M.; Lester, S.; Amano, J. A study of parasitic reactions

between NH₃ and TMGa or TMAI. *J. Electron. Mater.* **1996**, *25*, 1004–1008.

(30) Meyer, B. K.; Alves, H.; Hofmann, D. M.; Kriegseis, W.; Forster, D.; Bertram, F.; Christen, J.; Hoffmann, A.; Straßburg, M.; Dworzak, M.; Habocek, U.; Rodina, A. V. Bound exciton and donor–acceptor pair recombinations in ZnO. *Phys. Status Solidi B* **2004**, *241*, 231–260.

(31) Travnikov, V.; Freiberg, A.; Savikhin, S. Surface excitons in ZnO crystals. *J. Lumin.* **1990**, *47*, 107–112.

(32) *Handbook of luminescent semiconductor materials*; Bergman, L., McHale, J. L., Eds.; CRC Press: Boca Raton, FL, 2012.

(33) Wagner, M. R.; Callsen, G.; Reparaz, J. S.; Kirste, R.; Hoffmann, A.; Rodina, A. V.; Schleife, A.; Bechstedt, F.; Phillips, M. R. Effects of strain on the valence band structure and exciton-polariton energies in ZnO. *Phys. Rev. B: Condens. Matter Mater. Phys.* **2013**, *88*, 235210.

(34) Teke, A.; Özgür, Ü.; Doğan, S.; Gu, X.; Morkoç, H.; Nemeth, B.; Nause, J.; Everitt, H. Excitonic fine structure and recombination dynamics in single-crystalline ZnO. *Phys. Rev. B: Condens. Matter Mater. Phys.* **2004**, *70*, 195207.

(35) Thonke, K.; Gruber, T.; Teofilov, N.; Schönfelder, R.; Waag, A.; Sauer, R. Donor-acceptor pair transitions in ZnO substrate material. *Phys. B* **2001**, *308–310*, 945–948.

(36) Schirra, M.; Schneider, R.; Reiser, A.; Prinz, G. M.; Feneberg, M.; Biskupek, J.; Kaiser, U.; Krill, C. E.; Thonke, K.; Sauer, R. Stacking fault related 3.31eV luminescence at 130meV acceptors in zinc oxide. *Phys. Rev. B: Condens. Matter Mater. Phys.* **2008**, *77*, 125215.

(37) Wang, L.; Pu, Y.; Chen, Y.; Mo, C.; Fang, W.; Xiong, C.; Dai, J.; Jiang, F. MOCVD growth of ZnO films on Si(111) substrate using a thin AlN buffer layer. *J. Cryst. Growth* **2005**, *284*, 459–463.

(38) Zheng, C. D.; Wang, L.; Fang, W. Q.; Jiang, F. Y. Growth of ZnO films on Si (111) by metalorganic chemical vapor deposition with AlN and low-temperature ZnO double buffers. *Adv. Mater. Res.* **2013**, *652–654*, 594–598.

(39) Li, H.; Sadler, T. C.; Parbrook, P. J. AlN heteroepitaxy on sapphire by metalorganic vapour phase epitaxy using low temperature nucleation layers. *J. Cryst. Growth* **2013**, *383*, 72–78.

(40) Gonsalves, M.; Kim, W.; Narayanan, V.; Mahajan, S. Influence of AlN nucleation layer growth conditions on quality of GaN layers deposited on (0001) sapphire. *J. Cryst. Growth* **2002**, *240*, 347–354.

(41) Liu, J.-Q.; Qiu, Y.-X.; Wang, J.-F.; Xu, K.; Yang, H. Analysis of Modified Williamson-Hall Plots on GaN Layers. *Chin. Phys. Lett.* **2011**, *28*, 016101.

(42) Moram, M. A.; Vickers, M. E.; Kappers, M. J.; Humphreys, C. J. The effect of wafer curvature on x-ray rocking curves from gallium nitride films. *J. Appl. Phys.* **2008**, *103*, 093528.

(43) Dunn, C.; Kogh, E. Comparison of dislocation densities of primary and secondary recrystallization grains of Si-Fe. *Acta Metall.* **1957**, *5*, 548–554.

(44) Moram, M. A.; Vickers, M. E. X-ray diffraction of III-nitrides. *Rep. Prog. Phys.* **2009**, *72*, 036502.

(45) Studenikin, S. A.; Cocivera, M. Time-resolved luminescence and photoconductivity of polycrystalline ZnO films. *J. Appl. Phys.* **2002**, *91*, S060–S065.

(46) Egelhaaf, H.-J.; Oelkrug, D. Luminescence and nonradiative deactivation of excited states involving oxygen defect centers in polycrystalline ZnO. *J. Cryst. Growth* **1996**, *161*, 190–194.

(47) Xu, P.; Sun, Y.; Shi, C.; Xu, F.; Pan, H. The electronic structure and spectral properties of ZnO and its defects. *Nucl. Instrum. Methods Phys. Res., Sect. B* **2003**, *199*, 286–290.

(48) Lin, B.; Fu, Z.; Jia, Y. Green luminescent center in undoped zinc oxide films deposited on silicon substrates. *Appl. Phys. Lett.* **2001**, *79*, 943–945.

(49) Stoney, G. G. The tension of metallic films deposited by electrolysis. *Proceedings of the Royal Society of London. Series A, Containing Papers of a Mathematical and Physical Character* **1909**, *82*, 172–175.

(50) Wang, X.; Duan, Y.; Cui, J.; Zeng, Y. Crack free ZnO thick film on sapphire substrate without GaN template grown by MVPE. *Mater. Sci. Semicond. Process.* **2012**, *15*, 277–281.

(51) Azuhata, T.; Takesada, M.; Yagi, T.; Shikanai, A.; Chichibu, S.; Torii, K.; Nakamura, A.; Sota, T.; Cantwell, G.; Eason, D. B.; Litton, C. W. Brillouin scattering study of ZnO. *J. Appl. Phys.* **2003**, *94*, 968–972.

(52) Reeber, R. R.; Wang, K. Lattice Parameters and Thermal Expansion of Important Semiconductors and Their Substrates. *MRS Proceedings* **2000**, *622*, T6.35.1.

(53) Wortman, J. J.; Evans, R. A. Young's Modulus, Shear Modulus, and Poisson's Ratio in Silicon and Germanium. *J. Appl. Phys.* **1965**, *36*, 153–156.

(54) Okada, Y.; Tokumaru, Y. Precise determination of lattice parameter and thermal expansion coefficient of silicon between 300 and 1500 K. *J. Appl. Phys.* **1984**, *56*, 314–320.

(55) Wagner, M. R.; Bartel, T. P.; Kirste, R.; Hoffmann, A.; Sann, J.; Lautenschläger, S.; Meyer, B. K.; Kisielowski, C. Influence of substrate surface polarity on homoepitaxial growth of ZnO layers by chemical vapor deposition. *Phys. Rev. B: Condens. Matter Mater. Phys.* **2009**, *79*, 035307.

(56) Wrzesinski, J.; Fröhlich, D. Two-photon and three-photon spectroscopy of ZnO under uniaxial stress. *Phys. Rev. B: Condens. Matter Mater. Phys.* **1997**, *56*, 13087–13093.

(57) Wagner, J.-M.; Bechstedt, F. Properties of strained wurtzite GaN and AlN: Ab initio studies. *Phys. Rev. B: Condens. Matter Mater. Phys.* **2002**, *66*, 115202.

(58) Yoshikawa, H.; Adachi, S. Optical Constants of ZnO. *Jpn. J. Appl. Phys.* **1997**, *36*, 6237–6243.